ELSEVIER

Tectonophysics 258 (1996) 151–169

TECTONOPHYSICS

The effect of experimental and microstructural parameters on the transition from brittle failure to cataclastic flow of carbonate rocks

J. Renner, F. Rummel *

Institute for Geophysics, Research Group High-Pressure Metamorphism, Ruhr-University Bochum, 44780 Bochum, Germany

Received 30 January 1995; accepted 13 November 1995

Abstract

Triaxial compression tests were conducted on cold-pressed calcite, aragonite and limestone aggregates and on Solnhofen limestone specimens to study the effect of experimental and microstructural parameters on the transition from brittle failure to cataclastic flow. The tests were performed at confining pressures up to 195 MPa and at strain rates between $5 \cdot 10^{-4}$ s^{-1} and $5 \cdot 10^{-6}$ s^{-1}. Axial as well as volumetric strain were measured. Samples were produced by cold-pressing powders of crushed calcite and aragonite crystals and of crushed Solnhofen limestone. Sample porosity ranged between 5 and 25% and the average grain size varied between 5 and 400 μm.

For both the cold-pressed aggregates and the intact limestone specimens, the confining pressure at the transition from localized brittle failure to non-localized cataclastic flow decreases with increasing porosity and grain size. The transition is characterized by a zero work-hardening coefficient, by dilation for low porosity and compaction for high porosity rocks, by a constant ratio between axial stress and confining pressure, and by decreasing yield strength for increasing confining pressure. The experimental results disagree with the critical state concept over most of the porosity range investigated, and indicate non-associated material behaviour. These properties of the brittle–ductile transition are addressed on the basis of continuum mechanics or by models suggested for granular materials. The problems discussed and the results obtained are of fundamental interest to rock deformation and structural geology.

1. Introduction

The influence of porosity and grain size on brittle failure of rocks has been extensively investigated (e.g. Brace, 1961; Dunn et al., 1973; Hoshino, 1974; Olsson, 1974a; Friedman, 1976; Hugman and Friedman, 1979). However, only few experimental or theoretical studies exist for the transition from brittle failure to cataclastic flow (Dower, 1967; Hirth and Tullis, 1989; Fredrich et al., 1990; Zhang et al., 1990; Scott and Nielsen, 1991). Difficulties in interpretating the experiments arise from three reasons. First, because the effects of porosity and grain size are difficult to study independently in natural rocks, one of the two parameters usually is assumed to be

* Corresponding author.

SSDI 0040-1951(95)00192-1

of minor importance (Hugman and Friedman, 1979; Scott and Nielsen, 1991). Second, variations in other parameters such as chemical composition and cementation may obscure the observations. Third, volumetric strain should be measured to understand the micromechanisms active during cataclastic deformation (e.g. Brace et al., 1966; Edmond and Paterson, 1972; Gowd and Rummel, 1980; Fischer and Paterson, 1989). Hence, the effect of microstructural parameters on mechanisms for compaction and dilation have not yet been clearly shown.

We performed triaxial deformation tests, including volumetric strain measurements, on cold-pressed calcite and aragonite aggregates and intact limestone with different porosities and grain sizes. Our data allow to analyse the effects of confining pressure, strain-rate, porosity, grain size and mineralogy on mechanical properties. We consider both elastic and inelastic deformation and compare the data with predictions from both constitutive and micromechanical models.

2. Sample preparation

The Solnhofen limestone samples 20 mm in diameter and 40 mm long were cored from two blocks that have porosities of 5.5% and 3.7% and similar average grain sizes (Table 1a). Cold-pressed samples 22 mm in diameter and 44 mm long were produced by using powders of crushed calcite single crystals (Brilon, Germany, $99.5\%_{\text{weight}}$ $CaCO_3$), crushed aragonite single crystals (Horschenz, CSFR, $99.5\%_{\text{weight}}$ $CaCO_3$) and crushed Solnhofen limestone ($97.9\%_{\text{weight}}$ $CaCO_3$). Crushing in a tungsten carbide mortar resulted in average particle size fractions of 400 ± 100, 100 ± 25, 50 ± 15 and 15 ± 10 μm after sieving and washing (Table 1b).

We encountered a number of problems during cold-pressing: pore pressures (air) increased in the compaction cell and opposed compaction, friction between the samples and the compaction cell wall made it difficult to extract intact samples, and discing occurred when the radial constraint was removed because of stress relaxation. We minimized these problems by using continuous gas evacuation, lubricants between the sample surface and the polished die wall, and a compaction cell with conical internal bore. The axial stress applied during cold-pressing ranged up to 1300 MPa. At similar stresses calcite powders were easier to compact than aragonite powders and lower porosity samples were obtained from coarser-grained powders or powders with a wider distribution in particle size. Depending on the applied stress the sample porosities, ϕ_0 (calculated by comparing sample bulk densities with crystal densities), ranged between 5 and 25% (Table 1b). Die wall friction caused densities to vary by 1% per sample, with higher density in the upper portion of the sample.

The particle aspect ratios for all starting powders was 2 to 3, based on optical microscopy. Thin sections from cold-pressed samples show a preferred orientation of particles with their long axis perpendicular to the loading direction. For calcite, the shorter grain axis often is the c-axis (e.g., Fig. 1e). During cold-pressing, brittle deformation leads to a bimodal texture with 90 vol.% of large particles and 10 vol.% of small fragments with a few microns in diameter (e.g. Fig. 1a).

3. Experimental techniques

The specimens were evacuated for 24 h and then jacketed with a rubber sleeve prior to deformation. Tests were performed in a 400 MPa fluid-medium pressure vessel. Initial sample volume V_{hyd} and thus the initial sample porosity ϕ_i were determined from linear compressibilities due to hydrostatic loading prior to axial deformation (Brace, 1965). For the calculation of volume compressibilities we assumed isotropic and pure linear compaction for the intact limestone and the cold-pressed samples, respectively. The axial stress was applied by a servo-controlled loading system with piston displacement control.

During each deformation test the axial force, confining pressure σ_3 and piston displacement (axial strain ϵ_1) were digitally sampled ($\Delta t = 0.17$ s). Using a confining pressure compensation system, the volume change during deformation ΔV was measured (Gowd and Rummel, 1980). Volumetric strain θ was determined as $\theta = -\ln(1 - \Delta V/V_{\text{hyd}})$ with $\theta > 0$ for compaction and $\theta < 0$ for dilation. The axial stress σ_1 and the stress difference (differential stress) $\Delta\sigma = \sigma_1 - \sigma_3$ were corrected for the change

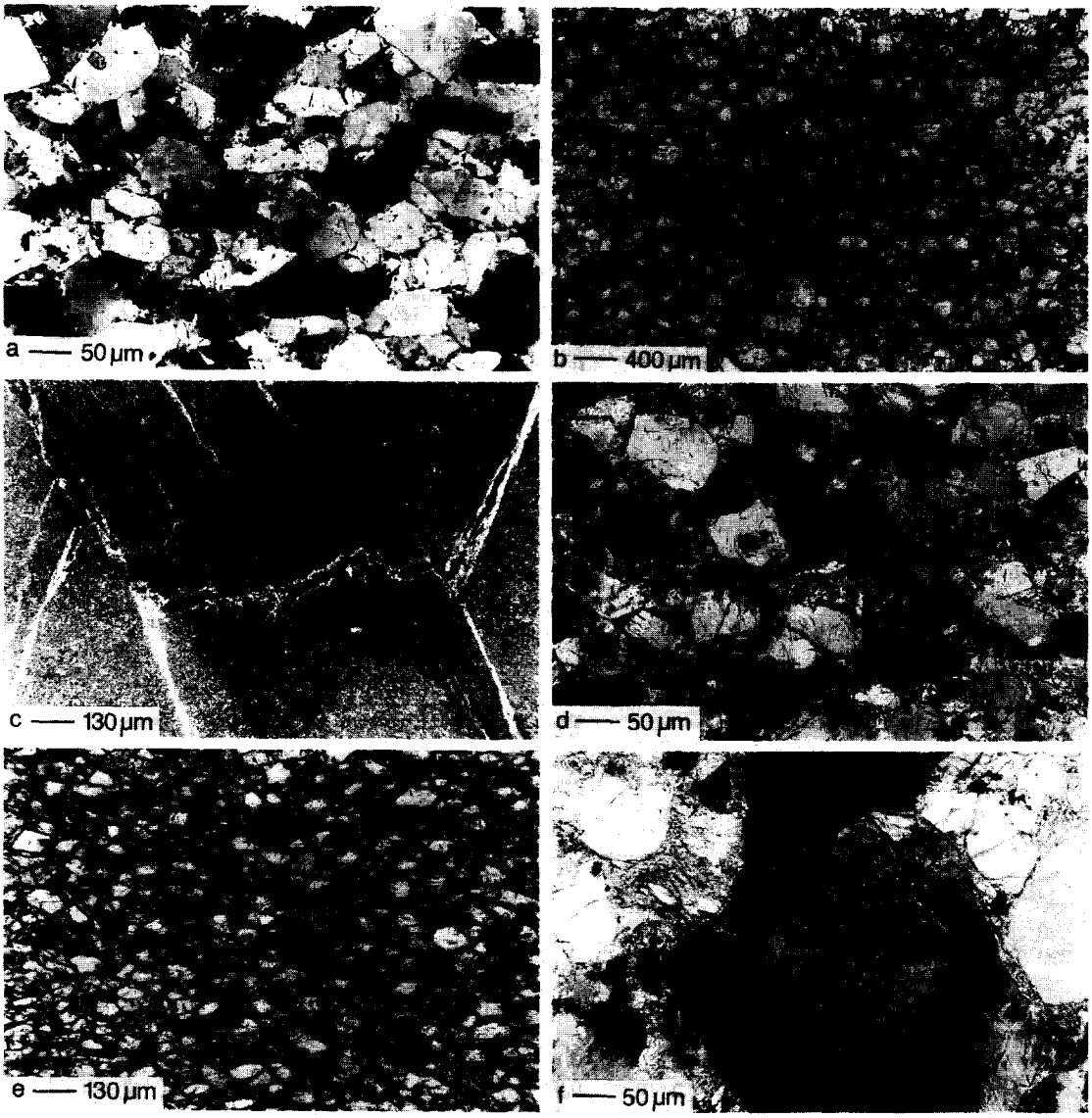

Fig. 1. Photomicrographs of various thin sections. Direction of axial stress is perpendicular to the long side of the figures. (a) Example of microstructure of a cold-pressed aragonite sample with about 12% porosity and 100 μm average grain size after cold-pressing prior to triaxial deformation (crossed polarizers). (b) Two major faults (coming parallel from top right corner) vanish in a zone of extensive cataclasis in the center of a cold-pressed aragonite sample (ar33) with a initial porosity of 11% and an average grain size of 390 μm deformed at 10 MPa confining pressure. First signs of a network of short shear faults are visible around the zone of extensive cataclasis. (c) Center of Solnhofen limestone sample (s112/4) deformed at 79.4 MPa confining pressure. Conjugate shear fractures meet and produce a complicate pattern typical for the transitional deformation field. (d) Microstructure of a cold-pressed aragonite sample (ar50, 11% initial porosity, 100 μm average grain size) deformed at 195 MPa confining pressure (crossed polarizers). The amount of fragments of a few microns surrounding the originally particles increases during non-localized deformation in the ductile deformation field. (e) Microstructure of a cold-pressed calcite sample (cc14, 7% initial porosity, 85 μm average grain size) deformed at 150 MPa confining pressure (crossed polarizers). Some properties of the microstructure resulting from cold-pressing are preserved during triaxial deformation: the preferred orientation of long grain axis perpendicular to the pressing direction; the frequent occurrence of cleavage plans as grain boundaries; the shorter grain axis being often the c-axis. The extensive mechanical twinning is obvious even without crossing polarizers. (f) Intra-granular deformation in an aragonite sample (ar13, 12% initial porosity, 390 μm average grain size) deformed at 195 MPa confining pressure (crossed polarizers). Apart from inter- and intragranular microcracks which are not related to crystallographic orientations one can observe a band of short, parallel, bended cleavage cracks, fine lamellae of mechanical twins and undulatory extinction due to (010)[100] dislocation glide.

Table 1
(a) Initial microstructural parameters, test conditions and results for intact Solnhofen limestone (sII, sIII) samples. (b) Initial microstructural parameters, test conditions and results for cold-pressed aragonite (ar), calcite (cc), and limestone (psl) samples

No.	Starting and test conditions					Test results: characteristics of inelastic deformation						
	$\bar{d}$ (μm)	ϕ_0 (%)	ϕ_1 (%)	σ_3 (MPa)	$\dot{\epsilon}_1$ (s^{-1})	m	h (MPa)	h' (MPa)	$\Delta\sigma_y$ (MPa)	$\Delta\sigma_d$ (MPa)	$\Delta\sigma_{max}$ (MPa)	comments
sII2/1	5	5.5	5.5	0	$1.0 \cdot 10^{-4}$	–	–	–	258	–	280	b1
sII2/2	5	5.5	5.4	50	$0.8 \cdot 10^{-5}$	−0.87	−2440	−4710	250	364	364	t1
sII2/3	5	5.5	5.5	0	$0.8 \cdot 10^{-5}$	–	–	–	260	–	278	b1
sII2/4	5	5.5	5.3	80	$1.0 \cdot 10^{-4}$	−0.55	−340	−340	334	387	387	t2
sII2/5	5	5.5	5.3	100	$0.8 \cdot 10^{-5}$	−0.34	220	120	270	396	396	d1
sII2/6	5	5.5	5.3	150	$1.0 \cdot 10^{-4}$	−0.14	660	560	275	401	468	d1
sII2/7	5	5.5	5.3	100	$1.0 \cdot 10^{-4}$	−0.38	0	−30	289	396	396	t2
sII2/8	5	5.5	5.3	50	$1.0 \cdot 10^{-4}$	−0.78	−1370	−5370	305	363	363	t1
sII2/9	5	5.5	5.2	195	$1.0 \cdot 10^{-4}$	−0.03	1000	870	259	444	508	d2
sII2/12	5	5.5	5.4	10	$5.0 \cdot 10^{-5}$	–	–	–	288	301	301	b1
sIII1/10	5	3.7	(3.7)	49.7	$3.7 \cdot 10^{-5}$	−0.98	−5050	−5370	312	422	422	t1
sIII2/1	5	3.7	3.4	99.2	$3.7 \cdot 10^{-5}$	−0.58	−280	−4160	315	451	451	t2
sIII2/2	5	3.7	3.7	0	$3.7 \cdot 10^{-5}$	–	–	–	312	369	369	b1
sIII2/4	5	3.7	3.5	79.4	$0.8 \cdot 10^{-5}$	−0.55	−690	−750	329	441	441	t2
sIII2/5	5	3.7	3.5	119.0	$0.9 \cdot 10^{-5}$	−0.26	190	160	340	452	463	d1
sIII2/6	5	3.7	3.4	148.8	$0.9 \cdot 10^{-5}$	−0.16	470	370	336	465	499	d1
sIII2/7	5	3.7	3.3	193.5	$1.0 \cdot 10^{-5}$	−0.04	810	750	314	482	532	d2
sIII2/8	5	3.7	3.5	29.8	$1.0 \cdot 10^{-5}$	–	–	–	317	412	412	t1
sIII2/9	5	3.7	3.5	64.5	$1.0 \cdot 10^{-5}$	−0.65	−5400	−11800	368	434	434	t1

No.	Cold pressing			Test conditions			Test results: characteristics of inelastic deformation						
	$\bar{d}$ (μm)	σ_{cp} (MPa)	ϕ_0 (%)	ϕ_1 (%)	σ_3 (MPa)	$\dot{\epsilon}_1$ (s^{-1})	m	h (MPa)	h' (MPa)	$\Delta\sigma_y$ (MPa)	$\Delta\sigma_d$ (MPa)	$\Delta\sigma_{max}$ (MPa)	comments
ar13	390	714	14.4	12.2	195	$5 \cdot 10^{-5}$	0.19	1690	1260	109	–	405	d2
ar14	390	102)	12.3	10.7	50	$5 \cdot 10^{-4}$	−0.3)	−180	−180	115	136	163	t2
ar21	390	718	14.4	12.3	150	$5 \cdot 10^{-5}$	0.15	1230	1080	110	–	337	d2
ar29	390	1256	11.1	9.4	50	$5 \cdot 10^{-5}$	−0.38	−350	−240	128	146	183	t2
ar33	390	1004	12.1	11.3	10	$5 \cdot 10^{-5}$	−0.98	−820	−820	52	43	60	t1
ar34	390	1004	11.9	10.4	50	$5 \cdot 10^{-5}$	−0.29	−250	−230	123	150	172	t2
ar35	390	1006	12.7	10.9	80	$5 \cdot 10^{-5}$	−0.05	90	−120	145	229	240	d1
ar36	390	997	12.5	10.2	150	$5 \cdot 10^{-5}$	0.10	1030	580	175	–	392	d2
ar38	390	1005	12.5	10.9	50	$5 \cdot 10^{-6}$	−0.33	−160	−110	110	125	162	t2
ar39	390	316	20.2	18.3	50	$5 \cdot 10^{-5}$	0.12	320	230	42	–	111	d2
ar56	390	1010	10.6	9.0	195	$5 \cdot 10^{-5}$	0.00	1500	1320	180	450	465	d2
ar57	390	610	14.1	12.7	50	$5 \cdot 10^{-5}$	−0.18	0	30	85	112	135	d1
ar46	100	1012	12.6	12.0	10	$5 \cdot 10^{-5}$	−0.94	−2860	−2860	59	43	74	t1
ar47	100	1012	12.7	11.6	50	$5 \cdot 10^{-5}$	−0.38	−750	−520	127	140	188	t1
ar48	100	1014	12.8	11.4	80	$5 \cdot 10^{-5}$	−0.26	−260	−190	157	214	244	t2
ar49	100	1006	12.6	11.0	150	$5 \cdot 10^{-5}$	−0.04	410	340	212	355	399	d1
ar50	100	1009	12.7	11.0	195	$5 \cdot 10^{-5}$	0.09	1040	870	200	–	466	d2
ar52	100	315	22.3	21.1	50	$5 \cdot 10^{-5}$	0.13	210	150	58	–	115	d2
ar53	100	616	16.7	15.6	50	$5 \cdot 10^{-5}$	−0.19	−80	−40	104	121	145	t2
ar54	65	1113	12.6	10.9	150	$5 \cdot 10^{-5}$	−0.08	290	290	232	325	406	d2
ar55	65	370	22.2	21.0	50	$5 \cdot 10^{-5}$	0.07	160	90	75	–	117	d1
ar22	15	709	16.3	15.1	50	$5 \cdot 10^{-5}$	−0.25	−370	−250	127	135	172	t1
ar25	15	700	17.6	16.5	80	$5 \cdot 10^{-5}$	−0.19	−110	−260	142	239	252	t1
ar26	15	717	17.8	16.3	150	$5 \cdot 10^{-5}$	0.09	780	490	159	–	389	d2
ar32	15	493	20.7	18.8	150	$5 \cdot 10^{-5}$	0.28	1230	920	114	–	328	d2
cc4	380	718	9.1	8.5	10	$5 \cdot 10^{-5}$	−0.95	−1220	−1680	57	61	79	t1

Table 1 (continued)

No.	Cold pressing			Test conditions			Test results: characteristics of inelastic deformation						
	$\bar{d}$ (μm)	σ_{cp} (MPa)	ϕ_0 (%)	ϕ_1 (%)	σ_3 (MPa)	$\dot{\epsilon}_1$ (s^{-1})	m	h (MPa)	h' (MPa)	$\Delta\sigma_y$ (MPa)	$\Delta\sigma_d$ (MPa)	$\Delta\sigma_{max}$ (MPa)	comments
cc6	380	1014	8.5	7.1	80	$5 \cdot 10^{-5}$	−0.26	160	180	136	226	274	d1
cc8	380	999	7.2	6.0	50	$5 \cdot 10^{-5}$	−0.52	−1050	−820	173	206	262	t2
cc16	380	420	12.0	11.1	50	$5 \cdot 10^{-5}$	−0.09	520	660	50	96	142	d1
cc17	380	421	11.8	10.9	80	$5 \cdot 10^{-5}$	−0.05	410	280	75	198	225	d1
cc18	380	419	11.9	10.4	150	$5 \cdot 10^{-5}$	0.20	1190	940	120	–	322	d2
cc19	380	1006	6.9	5.3	50	$5 \cdot 10^{-5}$	−0.61	−850	−560	181	206	256	t2
cc22	380	1005	7.6	5.7	50	$5 \cdot 10^{-5}$	−0.62	−1140	−1060	184	220	260	t2
cc10	85	521	14.7	12.6	50	$5 \cdot 10^{-5}$	−0.32	−220	−140	129	166	185	t2
cc11	85	522	14.8	13.8	10	$5 \cdot 10^{-5}$	−1.02	−3530	−4290	72	57	87	t2
cc12	85	519	14.7	12.1	150	$5 \cdot 10^{-5}$	0.21	1080	920	125	–	350	d2
cc13	85	904	10.3	7.6	50	$5 \cdot 10^{-5}$	−0.56	−1380	−1380	200	217	271	t1
cc14	85	1004	10.3	7.1	150	$5 \cdot 10^{-5}$	−0.02	900	620	207	411	464	d2
cc20	55	1002	11.3	8.9	50	$5 \cdot 10^{-5}$	−0.53	−890	−1340	188	191	265	t1
cc21	55	1001	11.4	7.9	150	$5 \cdot 10^{-5}$	−0.02	930	930	245	411	477	d2
cc5	15	532	16.2	15.0	50	$5 \cdot 10^{-5}$	−0.25	110	−90	89	171	188	t1
cc7	15	1290	9.0	7.9	80	$5 \cdot 10^{-5}$	−0.32	−60	−110	175	329	379	t1
psl11	320	712	9.8	8.7	40	$1 \cdot 10^{-4}$	−0.32	−330	−120	151	157	186	t2
psl12	320	1021	7.4	5.7	80	$1 \cdot 10^{-4}$	−0.38	−640	−330	224	254	326	t2
psl13	320	522	11.9	11.2	10	$1 \cdot 10^{-4}$	−0.88	−1160	−1160	50	71	78	t1
psl14	320	311	15.8	13.5	80	$1 \cdot 10^{-4}$	0	310	210	53	107	115	d1
psl22	320	984	7.7	6.2	50	$5 \cdot 10^{-5}$	−0.52	−3970	−3970	221	210	277	t1
psl23	320	564	11.8	10.9	10	$5 \cdot 10^{-5}$	−0.64	−2860	−3960	71	57	86	b2
psl24	320	518	12.4	11.0	50	$5 \cdot 10^{-5}$	−0.28	−180	−100	145	171	190	t2
psl25	320	518	12.5	10.2	150	$5 \cdot 10^{-5}$	0.21	1160	830	125	–	335	d2
psl26	320	497	12.8	11.0	80	$5 \cdot 10^{-5}$	−0.11	300	200	138	216	240	d1
psl10	180	713	11.9	10.1	80	$5 \cdot 10^{-5}$	−0.17	200	0	142	228	254	d1
psl27	75	443	15.1	13.3	80	$5 \cdot 10^{-5}$	−0.12	210	70	150	223	245	d1
psl28	75	454	14.8	13.1	50	$5 \cdot 10^{-5}$	−0.32	−270	−180	132	170	191	t2
psl29	75	446	14.9	12.5	150	$5 \cdot 10^{-5}$	0.26	1090	800	125	–	316	d2
psl30	75	995	8.5	6.7	50	$5 \cdot 10^{-5}$	−0.59	−1340	−2230	200	221	279	b2
psl21	15	713	12.5	10.7	150	$5 \cdot 10^{-5}$	0.09	640	560	168	–	390	d2

ϕ_0;ϕ_1 porosity at room pressure; initial porosity at specified confining pressure σ_3.
$\dot{\epsilon}_1$ strain rate.
$m = \partial\theta/\partial\epsilon_1$ dilatancy coefficient.
$h = \partial\Delta\sigma/\partial\epsilon_1$; $h' = \partial\sigma_w/\partial\epsilon_1 = h + \sigma_3 \cdot \partial m/\partial\epsilon_1$; apparent hardening coefficient; true hardening coefficient.
$\Delta\sigma_y$ yield stress ≡ stress at the onset of non-linearity in $\Delta\sigma$ vs. ϵ_1 curves.
$\Delta\sigma_d$ stress at the onset of dilation in θ vs. ϵ_1 curves.
$\Delta\sigma_{max}$ maximum differential stress up to 10% strain.
b1;b2 brittle field: axial splitting; single shear fracture.
t1;t2 transitional field: some shear fractures; multiple conjugate shear fractures.
d1;d2 ductile field: macroscopic non-localized deformation with central bulging; macroscopic non-localized deformation without central bulging.
$\bar{d}$ sl: average grain size; ar,cc,psl: average particle size of starting powder (for ar and cc equivalent to grain size, for psl equivalent to the size of coherent limestone aggregates).
σ_{cp} maximum axial stress applied during cold-pressing.

in cross-sectional area. The confining pressure ranged up to 195 MPa; the strain rate was varied between $5 \cdot 10^{-6}$ and $5 \cdot 10^{-4}$ s^{-1}, most tests being conducted at $5 \cdot 10^{-5}$ s^{-1} (Table 1). Accuracies are $\delta\Delta\sigma = \pm 1.0$ MPa for the stress difference, $\delta\sigma_3 = \pm 0.2$ MPa for the confining pressure, $\delta\epsilon_1 = \pm 0.02\%$ for the axial strain, and $\delta\theta = \pm 0.3\%$ for the volumetric strain.

4. Experimental results

Deformation tests were performed on 57 cold-pressed samples of aragonite (ar), calcite (cc) and crushed Solnhofen limestone (psl), and on 19 samples of intact Solnhofen limestone (sl). In general, brittle failure with sudden stress drops at peak stress is observed at low confining pressures and for samples with low porosities or small particle sizes. Ductile behaviour with distributed inelastic deformation and constant or increasing stress is typical for tests at high confining pressures and for samples with high porosities or large particle sizes. Brittle behaviour associated with significant dilation leads to macroscopic shear fracture, while ductile deformation accompanied by moderate dilation or even compaction results in barrel-shaped specimens without macroscopic fractures. Transitional behaviour is characterized by work-softening and dilation with multiple macroscopic shear fractures (Table 1).

4.1. Confining pressure

The effect of confining pressure on the strength of aragonite samples with an initial porosity of 11% and an average grain size of 100 μm is shown in Fig. 2. The slope of the initial linear portion of the $\Delta\sigma$ vs. ϵ_1 curves increases with confining pressure suggesting that the samples were compacting during hydrostatic loading prior to application of the axial load. Volumetric strain vs. axial strain curves demonstrate that compaction continues during axial loading. At low confining pressure ($\leq$ 150 MPa) compaction changes to dilation at small axial strain values. At high confining pressure ($\geq$ 150 MPa) compaction continues throughout inelastic deformation. The sample strength increases from 70 MPa at σ_3 = 10 MPa to greater than 450 MPa at σ_3 = 195 MPa. At all confining pressures, non-linear axial deformation begins at axial strains of about 1.5%. The brittle to ductile transition occurs at confining pressure between 80 and 150 MPa.

The increment of work per unit volume required for an increment of deformation is equivalent to the sum of the stress difference and the additional work done by the volumetric strain against the confining pressure and is given by $\Delta\sigma_W = \Delta\sigma + \sigma_3 \cdot \partial\theta/\partial\epsilon_1$ (Edmond and Paterson, 1972). Compaction is characterized by $\Delta\sigma_W > \Delta\sigma$, dilation by $\Delta\sigma_W < \Delta\sigma$. The onset ofdilation, as indicated by the cross-over of corresponding $\Delta\sigma$ vs. ϵ_1 and $\Delta\sigma_W$ vs. ϵ_1 curves, occurs at increasing axial strain with increasing confining pressure (Fig. 2).

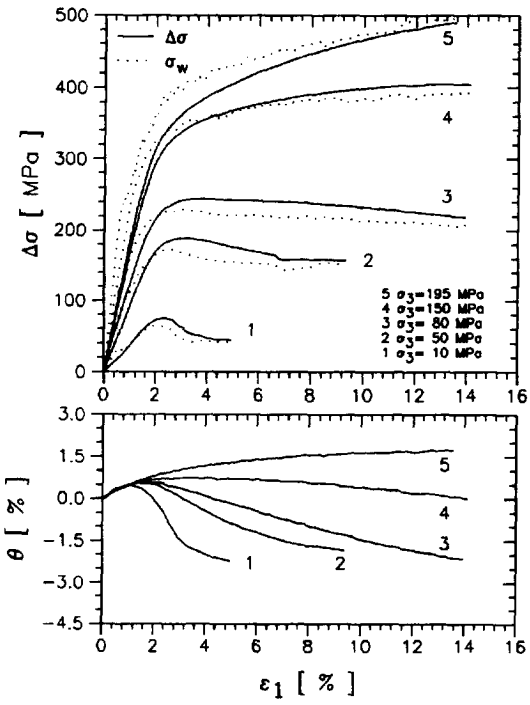

Fig. 2. Stress difference ($\Delta\sigma$), work of deformation ($\Delta\sigma_W$, dotted lines) and volumetric strain (θ) vs. axial strain (ϵ_1) curves showing the effect of confining pressure (σ_3) for cold-pressed aragonite rocks with approximately 11% initial porosity and 100 μm average grain size.

4.2. Porosity

The effect of porosity on the strength of cold-pressed aragonite and calcite samples and two intact Solnhofen limestone specimens is shown in Fig. 3. Aragonite samples subjected to a confining pressure of 50 MPa exhibit decreasing strength, a transition from brittle to ductile deformation and a transition from dilation to compaction with increasing sample porosity. Both cold-pressed calcite specimens subjected to a confining pressure of 150 MPa demonstrate work-hardening and compaction. The sample with lower porosity has a higher strength. The strength of intact limestone specimens subjected to 195 MPa also increases with decreasing porosity.

These low porosity samples deform at nearly constant volume.

4.3. Particle size

The effect of particle size on strength is shown in Fig. 4 for cold-pressed aragonite, calcite and limestone aggregates. The samples were deformed at confining pressures of 50, 80 and 150 MPa, respectively. The effect of particle size has a similar trend to that of porosity: the strength increases with decreasing particle size, and the samples with smaller particle size tend to show brittle behaviour. Because not only strength but also hardening behaviour is affected by particle size, the differences in strength due to particle size diminish with increasing strain. Compaction generally dominates for specimens with large particle size.

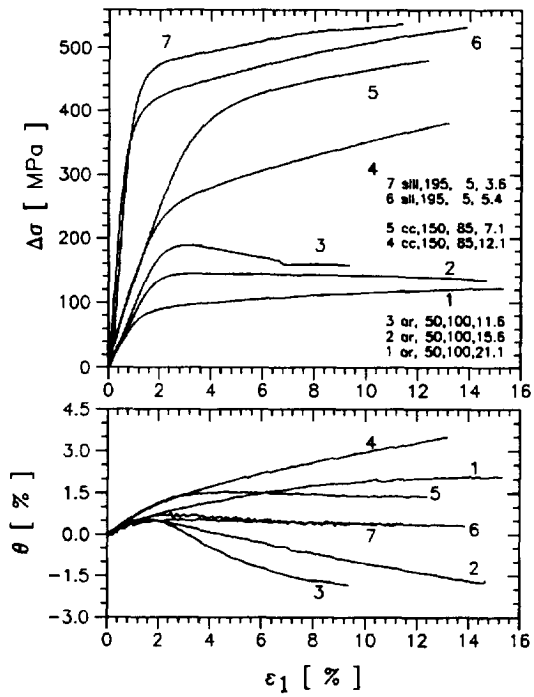

Fig. 3. Stress difference ($\Delta\sigma$) and volumetric strain (θ) vs. axial strain (ϵ_1) curves showing the effect of initial porosity for cold-pressed aragonite rocks (ar) with 100 μm average grain size at 50 MPa, cold-pressed calcite rocks (cc) with 85 μm average grain size at 150 MPa and intact Solnhofen limestone (sII, sIII) at 195 MPa confining pressure. [legend: curve no., material, confining pressure (MPa), initial porosity (%)], average grain size (μm)].

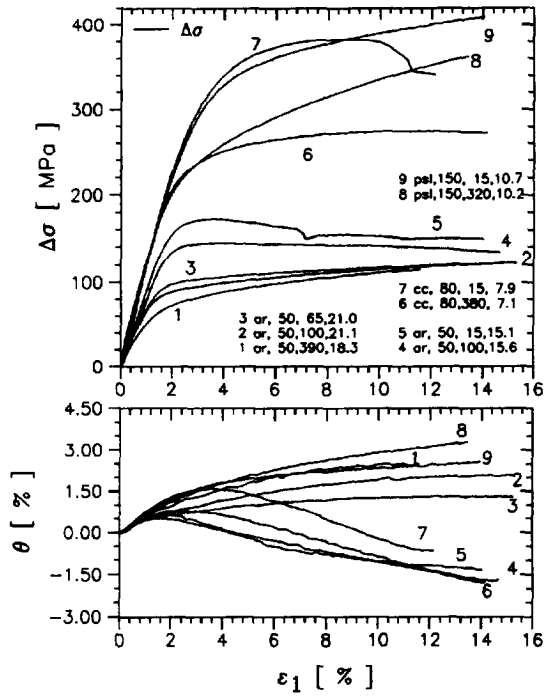

Fig. 4. Stress difference ($\Delta\sigma$) and volumetric strain (θ) vs. axial strain (ϵ_1) curves showing the effect of average particle size for cold-pressed aragonite rocks (ar) with 20 and 15% porosity at 50 MPa, cold-pressed calcite rocks (cc) with 7% porosity at 80 MPa and cold-pressed limestone (psl) with 10% porosity at 150 MPa confining pressure. [legend: curve no., material, confining pressure (MPa), initial porosity (%), average particle size (μm)].

4.4. Material

As a consequence of low porosities and small grain size, the Solnhofen limestone specimens show the highest strengths for almost all experimental conditions; cold-pressed aragonite aggregates tend to be stronger than cold-pressed calcite aggregates for similar porosity and particle size and identical confining pressure and strain rate (Table 1). In Fig. 5 some details of the material effect are shown. For samples of about 10% porosity and 400 μm particle size, cold-pressed Solnhofen limestone has a higher strength than aragonite and calcite samples at 50 MPa confining pressure, while the aragonite samples have a higher strength at 150 MPa. Similar stress–strain curves and almost identical volumetric strain are observed for the cold-pressed limestone and calcite samples at 150 MPa. Cold-pressed aragonite specimens are more dilatant than cold-pressed calcite

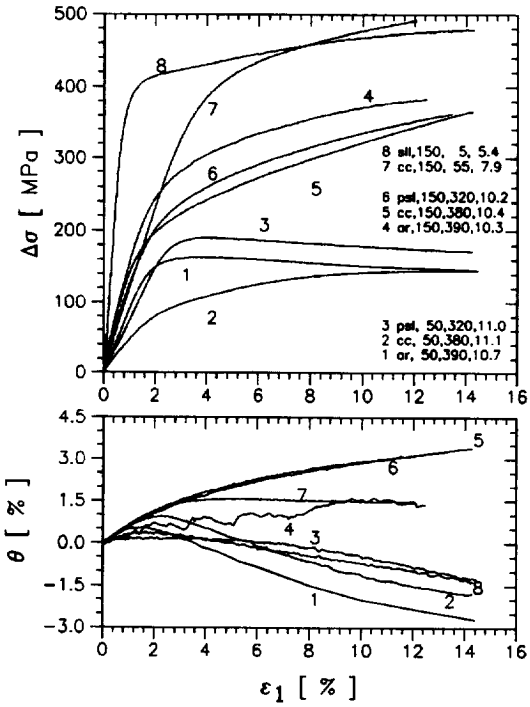

Fig. 5. Comparison of stress difference ($\Delta\sigma$) and volumetric strain (θ) vs. axial strain (ϵ_1) curves for microstructural similar cold-pressed rocks composed of calcite, aragonite and crushed limestone (cc, ar, psl) at 50 and 150 MPa, and for cold-pressed calcite (cc) and intact Solnhofen limestone (sll) at 150 MPa confining pressure.

and limestone specimens at similar confining pressures. Comparable stress differences are observed as the initial porosity difference between the finer grained intact limestone ($\phi_i = 5.4\%$) and the cold-pressed calcite sample ($\phi_i = 7.9\%$) decreases during ductile deformation at $\sigma_3 = 150$ MPa.

4.5. Strain rate

Considering experimental uncertainties, stress difference and volumetric strain are nearly unaffected by strain rate changes from $5 \cdot 10^{-4}$ to $5 \cdot 10^{-6}$ s^{-1} (Table 1). Apparently, in the investigated range of strain-rate the transition from brittle to ductile deformation is strain-rate insensitive for porous carbonate rocks at room temperature.

4.6. Optical microscopy

Thin sections of samples deformed at low and intermediate confining pressures contain either single brittle shear fractures or conjugate shear fracture systems typical of transitional deformation (Fig. 1b, c). With increasing confining pressure the localized fractures branch particularly in the specimen centre. In the central region we observe grains with crushed corners and networks of intergranular shear bands extending over a few grain diameters. Samples deformed in the "ductile" field show microfractures and small fragments of a few microns in diameter more homogeneously distributed. The original particles are surrounded by seams of cataclastic fragments (Fig. 1d, e).

Deformed calcite samples show pronounced mechanical twinning compared to undeformed specimens. Aragonite grains, especially when deformed at high stress differences (≥ 350 MPa), exhibit (010) cleavage fractures, fine lamellae of mechanical {110}-twins and undulatory extinction (Fig. 1f). Kink-band orientations in aragonite measured with universal-stage microscopy suggest two dislocation glide systems: one is the well-known system (010) [100] (Veit, 1922); the other system (001) [010] has not been described so far to our knowledge.

5. Discussion of experimental results

While elastic deformation behaviour is easily described by Young's modulus $E = \partial\Delta\sigma/\partial\epsilon_1$ and Poisson's ratio $\upsilon = -\partial\epsilon_2/\partial\epsilon_1$, characterization of inelastic deformation is more complicated. Curvatures and discontinuities in stress–strain and volumetric strain curves are significant and must be explained. The analysis uses a number of macroscopic property characteristics (e.g., Rummel, 1982):

- $\Delta\sigma_{max}$ is the maximum stress difference observed during the first 10% of axial deformation.
- The conventional yield strength, $\Delta\sigma_y$, is the stress difference at which $\Delta\sigma$ vs. ϵ_1 curves become non-linear. The initial non-linearity for stresses smaller than about 5 MPa and strains smaller than about 0.2% which presumably occurs due to the closure of existing microcracks (Walsh, 1965) is not considered for the determination of $\Delta\sigma_y$.
- The stress difference at the onset of dilation, $\Delta\sigma_d$, is determined when the differential $\partial\theta/\partial\epsilon_1$ changes sign from positive to negative.
- The coefficient of internal friction is the gradient of the yield surface, which is here represented

following Rudnicki and Rice (1975) by a plot of octahedral shear stress ($\tau = \Delta\sigma/\sqrt{3}$) vs. mean stress [$\bar{\sigma} = (\Delta\sigma + 3 \cdot \sigma_3)/3$] at yielding. In theory, yielding should be recognized as the first deviation of material deformation behaviour from Hooke's law which linearily relates stress and strain in three dimensions. In practice, the determination of the yield point is not unique. Restricting to the axial loading direction, the yield point often is chosen as the onset of non-linearity in $\Delta\sigma$ vs. ϵ_1 curves, i.e. $\tau_y = \Delta\sigma_y/\sqrt{3}$ and $\bar{\sigma}_y = (\Delta\sigma_y + 3 \cdot \sigma_3)/3$, leading to a friction coefficient μ_y (e.g. Gowd and Rummel, 1980; Bernabe and Brace, 1990; Khan et al., 1991). Considering strain in the radial direction, the yield point is determined as the onset of non-linearity in $\Delta\sigma$ vs. θ or θ vs. ϵ_1 curves (e.g. Brace et al., 1966; Gowd and Rummel, 1980; Khan et al., 1991). However, the onset of non-linearity in θ vs. ϵ_1 curves is difficult to determine for porous or pre-cracked rocks, which often do not show an initial linear elastic relation (Paterson, 1978), or for test conditions which only produce linear θ vs. ϵ_1 curves (Bernabe and Brace, 1990). To a certain extent, this difficulty may be resolved by comparing measured volumetric strains under triaxial loads with volume compaction under hydrostatic pressure (Schock et al., 1973). Fredrich et al. (1989) used the stress difference at the onset of dilation, $\Delta\sigma_d$, i.e. $\tau_d = \Delta\sigma_d/\sqrt{3}$ and $\bar{\sigma}_d = (\Delta\sigma_d + 3 \cdot \sigma_3)/3$, to estimate a coefficient of internal friction, μ_d.

In the case of smooth deformation curves the change of curvature may be an indication of a change in deformation processes. A first approach to characterize the inelastic deformation behaviour after yielding, but prior to strong curvature changes, is to introduce the following coefficients (compare Edmond and Paterson, 1972; Fredrich et al., 1989):

- $h = \partial\Delta\sigma/\partial\epsilon_1$ (apparent work-hardening coefficient);
- $h' = \partial\sigma_W/\partial\epsilon_1 = h + \sigma_3 \cdot \partial^2\theta/\partial\epsilon_1^2$ (true work-hardening coefficient);
- $m = \partial\theta/\partial\epsilon_1$ (dilatancy coefficient).

5.1. Comparison with previous work

Strength, volume changes, and deformation and fracture features of Solnhofen limestone (sII, ϕ = 5.5%) agree well with those of Rutter (1972) and Edmond and Paterson (1972) for limestones with similar porosity and grain size. The results described by Heard (1960) and Byerlee (1968) for Solnhofen limestone (ϕ = 1.7 and 4.8%) and our data on Solnhofen limestone (ϕ = 3.7 and 5.5%) complement the data set which uniquely shows the increase of strength with decreasing porosity for intact sedimentary rocks. The fact that calcite marbles with porosities smaller than 1% yield lower strength values (e.g. Rummel, 1982) is due to different grain sizes, grain-size distributions and grain defects (Hugman and Friedman, 1979; Fredrich et al., 1990).

Cold-pressed calcite samples show deformation behaviour similar to intact natural rock specimens of comparable grain size and porosity (Hugman and Friedman, 1979). Cold-pressed aragonite samples are stronger than cold-pressed calcite samples but the difference is less than that between natural calcite and dolomite rocks (Handin and Hager, 1957; Hugman and Friedman, 1979; Rummel, 1982).

5.2. Characteristics of elastic and inelastic deformation behaviour

5.2.1. Elastic parameters

The most conspicuous difference between the deformation of intact limestone and cold-pressed calcite/aragonite samples is in the elastic range. Cold-pressed samples have small Young's moduli. However, Young's moduli increase with increasing confining pressure and with decreasing porosity (Table 1, Figs. 2 and 3). The increase of Young's modulus with pressure may be explained by the closure of microcracks or pores (e.g. Walsh, 1965; Budiansky and O'Connell, 1976). The increase of Young's modulus with decreasing porosity is related to the increase of solid material per unit cross-section (Digby, 1981; Walton, 1987). Poisson's ratio ν is affected less by porosity, grain size and pressure. The average value for the tested materials is $\nu = 0.23 \pm 0.10$.

5.2.2. Internal friction coefficients

Fig. 6 presents yield surfaces for the onset of non-linearity in $\Delta\sigma$ vs. ϵ_1 and for the onset of dilation in θ vs. ϵ_1 curves ($\bar{\sigma}_y$, τ_y and $\bar{\sigma}_d$, τ_d, respectively). The data originate from tests on sam-

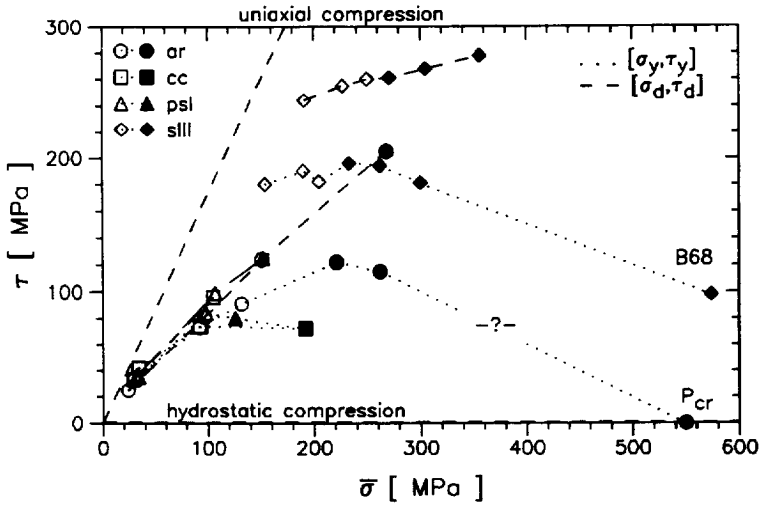

Fig. 6. Comparison of yield surfaces deduced from the onset of non-linearity in $\Delta\sigma$ vs. ϵ_1 curves (dotted lines) and from the onset of dilation in θ vs. ϵ_1 curves (dashed lines) for the rocks investigated (open symbols: localized deformation, closed symbols: non-localized deformation). The Solnhofen limestone data (sIII) are supplemented with a data point from Byerlee (1968) (B68). The extrapolation (–?–) qualitatively indicates the relation of yield surfaces and critical hydrostatic pressures P_{cr} (Zhang et al., 1990).

ples with similar porosity and grain size and deformed at various confining pressures. The yield surfaces for $\Delta\sigma$ vs. ϵ_1 are concave downwards with a change from positive to negative slope close to the transition from macroscopic localized to non-localized deformation. In contrast, yield surfaces for θ vs. ϵ_1 exclusively show positive slopes, which may slightly decrease with increasing mean stress. These qualitative results are independent of the different materials, cold-pressed calcite or aragonite samples, cold-pressed or intact Solnhofen limestone specimens.

The relation between the internal friction coefficient μ_d and porosity is given in Fig. 7. The data presented show an increase of μ_d with increasing porosity and a small increase with increasing grain size. A similar porosity relation exists for quartzitic rocks such as Gosford sandstone ($\phi = 13\%$; Edmond and Paterson, 1972; EP72 gs), Buntsandstone ($\phi = 15\%$; Gowd and Rummel, 1980; GR80 bs), or Berea sandstone ($\phi = 18.6 \pm 0.3\%$; Bernabe and Brace, 1990; BB90 bs).

5.2.3. Dilatancy coefficients

Dilatancy coefficients versus initial porosity are shown in Fig. 8. With increasing porosity the boundary between data from tests with and without macroscopic localization is marked by increasing dilatancy coefficients. For porosities $< 20\%$ the boundary corresponds to negative m values. For the three above cited sandstones a qualitatively similar dependence of the dilatancy coefficient at the brittle–ductile transition on porosity is found, which can be extended to

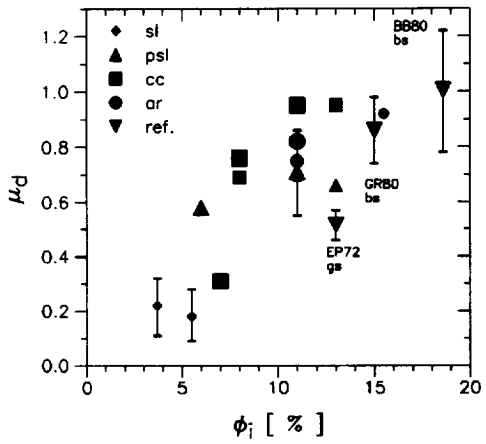

Fig. 7. Internal friction coefficients μ_d calculated from the onset of dilation increase with increasing initial porosity ϕ_i. For carbonates symbol size qualitatively corresponds to average particle size. Data points deduced from experiments on quartzitic rocks are given for comparison (references see text). Vertical bars indicate variations with confining pressure.

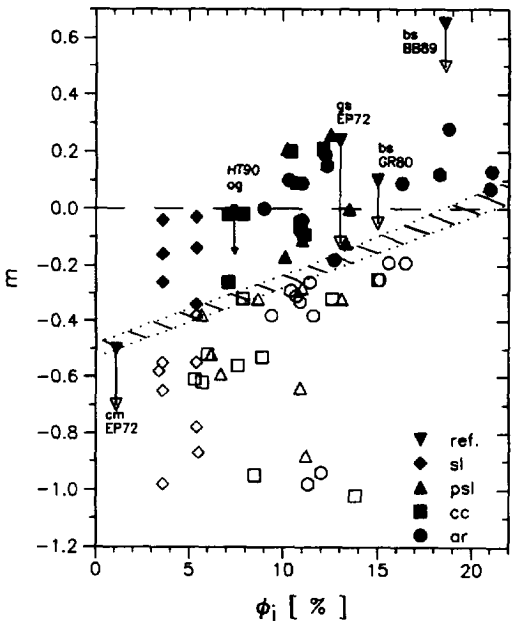

Fig. 8. With increasing initial porosity ϕ_i, the brittle–ductile transition (indicated by the shaded area) occurs at increasing dilatancy coefficients m (open symbols: localized deformation; closed symbols: non-localized deformation). Data of Carrara marble (Edmond and Paterson, 1972; EP72 cm) extend the observations to carbonates of very low porosity. Experiments on sandstones (EP72 gs; GR80 bs; BB90 bs) yield an increase of dilatancy coefficients at the transition with porosity, too (references see text). Microscopical observations of Hirth and Tullis (1989) on Oughtibridge ganister ($\phi = 7.4\%$; HT89 og) suggesting that pore collapse occurs at pressures in excess of the brittle–ductile transition pressure extend the trend observed for the sandstones towards lower porosities.

lower porosities by the observation of Hirth and Tullis (1989) on Oughtibridge ganister ($\phi = 7.4\%$; HT89 og) that pore collapse occurs at pressures in excess of the brittle–ductile transition pressure (Fig. 8). From Table 1 a further relationship can be found between the macroscopic appearance of deformed specimens and the measured dilatancy coefficients. In the ductile field extensive bulging (d1) is limited to dilatant behaviour ($m < 0$), whereas the cylindrical shape (d2) is essentially preserved when inelastic deformation is characterized by compaction.

5.2.4. Hardening coefficients

The values of h' versus initial porosity are shown in Fig. 9. Non-localized deformation directly correlates with work hardening ($h' > 0$). Macroscopic fault planes do not appear in specimens from tests terminated when the σ_W vs. ϵ_1 curves were characterized by positive gradients. Therefore, work hardening coefficients $h' \approx 0$ seem to determine the boundary between brittle fracture and cataclastic flow, indicating the equivalence of energetic and macroscopic stability. Since the signs of h' and h are identical (in all but two cases, see Table 1), the trends of either $\Delta\sigma$ vs. ϵ_1 or σ_W vs. $\epsilon_1$curves could be used to characterize the deformation.

When both h' and h are positive, h' values generally are smaller than h. However, when both parameters are negative, h' values generally are greater than h (Table 1). This correlation indicates a predominance of non-zero second derivatives $\partial^2\theta/\partial\epsilon_1^2$ in the relationship between h' and h: $h' = h + \sigma_3 \cdot \partial^2\theta/\partial\epsilon_1^2$. In the ductile field ($h'$, $h > 0$) compaction rate diminishes with increasing axial strain during non-localized inelastic deformation (e.g., Fig. 3, curve 1). In the brittle field (h', $h < 0$) dilation, once initiated, progresses until macroscopic faulting occurs (e.g. Fig. 2, curve 1).

5.2.5. Transition pressure and stress ratio

Interpolating work hardening coefficients to $h' \approx 0$, experimental lower and upper bounds for the brittle–ductile transition pressure σ_{trans} as a function

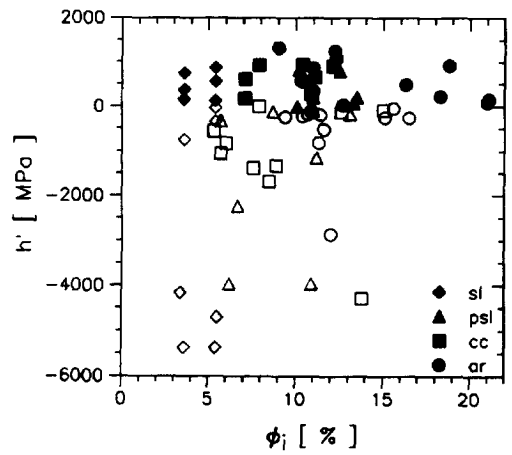

Fig. 9. Hardening coefficients h' versus initial porosity ϕ_i (open symbols: localized deformation; closed symbols: non-localized deformation). Localization was not found when tests where terminated at positive gradients h'.

of initial porosity are given in Fig. 10. For all materials tested the transition pressure predominantly increases with decreasing porosity and subordinatly with decreasing grain size. The data points for cold-pressed calcite extend the trend of intact Solnhofen limestone to higher porosities. Plumb (1994) shows a similar porosity dependence of the confining pressure at the brittle–ductile transition for clastic rocks with porosities varying from 0 to 40% and clay mineral volume fractions up to 72%.

Fig. 11 shows the maximum stress difference $\Delta\sigma_{max}$ as a function of confining pressure. Unique lines separate the fields of localized and non-localized deformation for each material. The data for both intact Solnhofen limestones yield a stress ratio of $\lambda_{sl} = \sigma_3/\sigma_{max} \approx 0.19$ in agreement with the stress ratio estimated by Fredrich et al. (1990) for natural

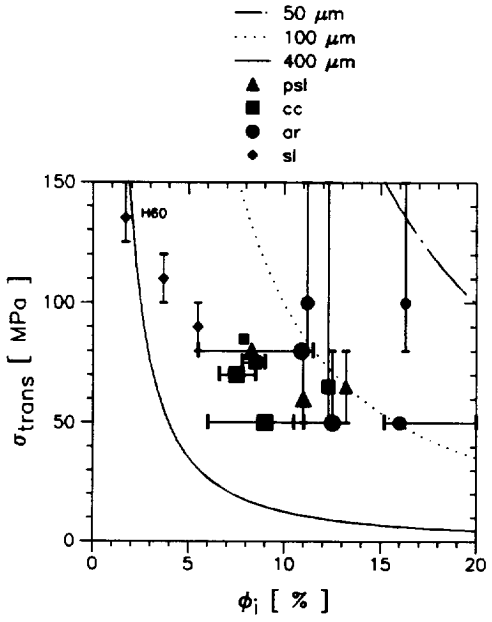

Fig. 10. The brittle–ductile transition in the $\sigma_3 - \phi_i$-field for the carbonates examined (symbol size qualitatively corresponds to average particle size; H60: result from Heard (1960) on Solnhofen limestone). Bars indicate how the transition is bracketed by two actual experiments, whereas data points are derived from interpolations of the dependence of hardening on confining pressure or porosity to $h' = h = 0$. The transition pressure σ_{trans} is a decreasing function of porosity and average particle size. Given curves are calculated after Zhang et al., 1990, from $\sigma_{trans} = 3\lambda\bar{\sigma}_{trans}/(1+2\lambda) \equiv 3\lambda P_{cr}/(1+2\lambda) = A\cdot(\phi\bar{d})^{-3/2}$ with $A = 6.3\cdot 10^{-6}$ MPa $\mu m^{3/2}$ and $\bar{d} = 50$, 100 and 400 μm respectively.

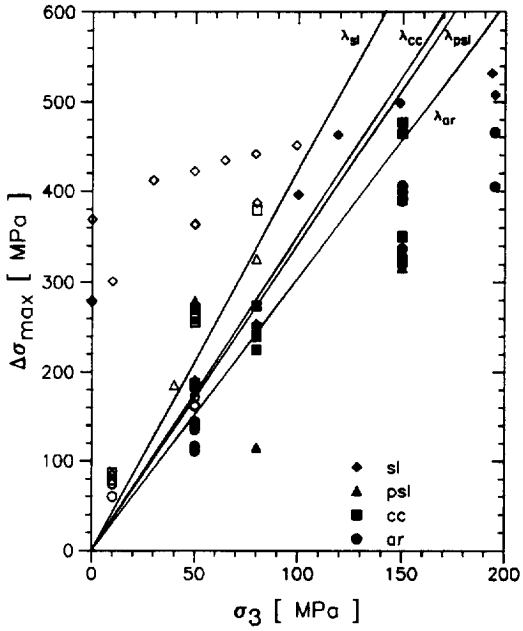

Fig. 11. Maximum stress differences $\Delta\sigma_{max}$ (observed for $\epsilon_1 \leq 10\%$) versus confining pressure σ_3. Lines indicate that the brittle–ductile transition occurs at constant stress ratios (open symbols: localized deformation, closed symbols: non-localized deformation).

carbonates of different grain sizes. For cold-pressed limestone and calcite samples $\lambda_{psl} \approx \lambda_{cc} \approx 0.22$. Cold-pressed aragonite specimens yield a value of $\lambda_{ar} \approx 0.25$. Similarly, stress ratios at the brittle–ductile transition for fine to coarse grained sandstones and quartzites with porosities up to 60% are 0.2 to 0.3 (Kwasniewski, 1989; Rutter and Hadizadeh, 1991).

5.3. Experimental constraints on constitutive equations

A basic question for the formulation of a constitutive equation in plasticity is how hardening and dilatancy coefficients are related. In critical state mechanics it is assumed that depending on its initial porosity and on the applied confining pressure an axially compressed material exhibits simultaneously either compaction and work-hardening or dilation and work-softening until the critical state is reached which allows perfectly plastic deformation at constant stress difference and volume. The behaviour of

soils is adequately described by critical state mechanics (e.g. Schofield and Wroth, 1968), therefore, it has been attempted to apply it to rocks, too (e.g. Gerogiannopoulos and Brown, 1978). For the carbonate aggregates, investigated signs of the hardening and dilatancy coefficients are not strictly the same and we do not observe perfectly plastic behaviour (i.e. $h = 0$, $m = 0$) in the range of confining pressures of 50 to 195 MPa and porosities of up to 20%. Therefore, application of critical state mechanics to low porosity rocks is not justified although good numerical fits may be achieved (Gerogiannopoulos and Brown, 1978). However, critical states can not be excluded for confining pressures below 50 MPa and porosities of more than 20%.

The classical assumption of plasticity that stresses and plastic strain increments are co-axial results in the coincidence of plastic strain increments with the normals of the yield surfaces, which is known as the normality rule (e.g. Chakrabarty, 1987; Hobbs et al., 1990). Materials obeying this rule exhibit so-called associated behaviour. However, for materials deforming by micromechanisms that are frictional and dilational this rule is not expected to be valid and the appropriate behaviour is called non-associated. In terms of experimentally accessible parameters the validity of the normality rule means that the dilatancy factor $\beta = \sqrt{3} \cdot m/(m-3)$ and the coefficient of internal friction μ are identical. In order not to be restrictive in the choice of the yield surface when carrying out this comparison we calculated not only the coefficients of internal friction μ_y and μ_d explained above but also a coefficient μ_{max} from the pressure dependence of the maximum stress difference, $\Delta\sigma_{max}$. Corresponding dilation factors β_y, β_d, and β_{max} were determined as local gradients at the stress differences $\Delta\sigma_y$, $\Delta\sigma_d$, and $\Delta\sigma_{max}$, respectively:

(1) At the onset of non-linearity in $\Delta\sigma$ vs. ϵ_1 curves a net volume increase with $\beta_y > 0$ is observed for a few specimens deformed at $\sigma_3 = 10$ MPa, only (e.g. Table 3). For all other cases β_y is negative resembling that specimens are still compacting. In contrast, the coefficient of internal friction μ_y changes sign from positive to negative at much higher confining pressures close to the brittle–ductile transition (Fig. 6; Tables 2 and 3).

(2) Whereas at the onset of dilatancy $\beta_d = 0$ per definition the coefficient of internal friction μ_d is a function of porosity and without exeption positive (Fig. 7; Tables 2 and 3).

Table 2
Lower and upper limits of experimentally determined dilatancy factor β and internal friction coefficients μ_y, μ_d and μ_{max}

Mat.	β	μ_y	μ_d	μ_{max}
ar	−0.19, 0.43	−0.17, 0.63	0.69, 0.92	0.57, 0.84
cc	−0.12, 0.43	−0.05, 0.54	0.31, 0.95	0.55, 0.83
psl	−0.19, 0.40	−0.20, 0.80	0.58, 0.84	0.44, 0.80
sl	0.00, 0.43	−0.34, 0.28	0.13, 0.31	0.23, 0.73

(3) When true peak stresses are observed, $\beta_{max} > 0$ indicating net volume increase. When specimens hardened throughout the experiment, $\beta_{max} > 0$ (i.e. $m < 0$) as well as $\beta_{max} < 0$ (i.e. $m > 0$) is observed (Tables 1 and 3). However, the pressure dependence of the deformation behaviour of the carbonate aggregates investigated expresses in positive values of the coefficient of internal friction μ_{max} (Tables 2 and 3).

Therefore, it has to be followed, that the normality rule is not valid for the carbonate aggregates investigated but that their behaviour is non-associated.

Rudnicki and Rice (1975) derived constitutive equations assuming non-associated material behaviour. By relating macroscopic localization to constitutive instability these equations provide a prediction of the failure mode (i.e., localized or non-localized) when —besides elastic constants — the yield surface and the relation between stresses and inelastic strains of the material under consideration are known. The predictions are made as critical hardening moduli normalized to elastic shear modulus $\tilde{h}/G$ for an isotropic hardening (formula 20 in Rudnicki and Rice, 1975) and for a yield vertex (i.e. non-isotropic hardening, appendix II in Rudnicki and Rice, 1975) model. Normalized hardening coefficients — experimentally determined and for isotropic hardening in the case of triaxial compression theoretically predicted — are listed in Table 3. For each choice of yield surface (μ_y, μ_d and μ_{max}) localization is predicted correctly for work-softening only, but in the brittle and transitional field where identical values are expected the quantitative agreement between experimental and theoretical results is poor. Nevertheless, both, experimental and theoretical results,

Table 3
Examples of corresponding coefficients of internal friction μ and dilatancy factors β. Deformational characteristics derived from the present experiments and theoretical predictions of critical ratios of hardening coefficients and shear moduli after Rudnicki and Rice (1975). Experimental and theoretical hardening coefficients generally exhibit similar dependences on (a) confining pressure, (b) porosity and (c) grain size. (Note: Hardening moduli $\tilde{h}$ calculated from formula 20 in Rudnicki and Rice (1975) are related to hardening coefficients h by $h/G = (3-m)2\cdot(\tilde{h}/G)/(1+\tilde{h}/G)$. Because the point of localization can not be determined from a stress–strain curve alone, the linearly approximated post peak relations between plastic strain increments β were used in the calculation instead of the local gradients β_y, β_y and β_{max}. The "*" denotes dilatancy factors and friction coefficients with $\beta+\mu > \sqrt{3}/2$ For these values localization is predicted to develop subparallel to the direction of the maximum stress difference and a geometry factor $N = -2/\sqrt{3}$ had to be used. Owing to the observation of dipping macroscopic faults, $N = 1/\sqrt{3}$ was used as for the case $\beta+\mu < \sqrt{3}/2$.)

(a)

	ar, $\bar{d}$ = 100 μm, $\bar{\phi}_i \approx 11\%$					slII, $\bar{d}$ = 5 μm, $\bar{\phi}_i \approx 3.5\%$				
σ_3 [MPa]	10	50	80	150	195	49.7	79.4	119.0	148.8	193.5
μ_y	0.63	0.50	0.36	0.09	−0.17	0.28	0.21	0.03	−0.20	−0.34
β_y	0.06	−0.10	−0.12	−0.16	−0.21	−0.18	−0.57	−0.49	−0.51	−0.31
ν_d	0.77	0.79	0.75	0.69	–	0.31	0.24	0.19	0.20	0.20
β_d	0	0	0	0	0	0	0	0	0	0
μ_{max}	0.84	0.75	0.70	0.65	0.57	0.30	0.24	0.39	0.42	0.34
β_{max}	0.30	0.26	0.17	0.02	−0.05	0.34	0.12	0.14	0.09	0.02
ν	0.18	0.21	0.24	0.22	0.22	0.36	0.13	0.17	0.12	0.27
G (GPa)	1.7	3.8	4.8	6.9	7.8	23.5	28.3	23.9	21.9	20.9
β	0.41	0.19	0.14	0.02	−0.05	0.43	0.27	0.14	0.09	0.02
com.	t1	t1	t2	d1	d2	t1	t2	d1	d1	d2
$(h/G)_{exp}$	−1.73	−0.20	−0.05	0.06	0.13	−0.21	−0.02	0.01	0.02	0.04
$(h_y/G)_{RR75}$	−1.93 *	−1.02 *	−0.82	−0.45	−0.26	−1.60	−0.79	−0.50	−0.28	−0.20
$(h_d/G)_{RR75}$	−2.26 *	−1.29 *	−1.12 *	−0.73	–	−1.69	−0.82	−0.62	−0.54	−0.54
$(h_{max}/G)_{RR75}$	−2.24 *	−1.25 *	−1.08 *	−0.72	−0.56	−1.65	−0.82	−0.78	−0.67	−0.62

(b)

	psl, 320 μm, 50 MPa		cc, 380 μm, 50 MPa		d [μm] (c) ar, 50 MPa, ≈ 11%	
$\bar{\phi}_i$(%)	11	6	11	6–8	390	100
μ_y	−0.14	0.03	0.37	0.48	0.53	0.50
β_y	−0.14	0.00	−0.11	0.09	0.00	−0.51
μ_d	0.58	0.58	0.95	0.76	0.82	0.79
β_d	0	0	0	0	0	0
μ_{max}	0.71	0.61	0.83	0.65	0.77	0.75
β_{max}	0.16	0.30	0.05	0.31	0.18	0.26
ν	0.15	0.17	0.15	0.39	0.24	0.21
G (GPa)	3.4	3.2	4.1	1.6	3.7	3.8
β	0.15	0.26	0.05	0.29	0.16	0.19
com.	t2	t1	d1	t2	t2	t1
$(h/G)_{exp}$	−1.19	−0.06	−0.21	0.32	−0.21	0.32
$(h_y/G)_{RR75}$	−0.37	−0.60	−0.77	−1.17	−1.01	−1.02
$(h_d/G)_{RR75}$	−0.94	−1.21	−0.91 *	−1.54 *	−1.24 *	−1.29 *
$(h_{max}/G)_{RR75}$	−1.04 *	−1.25	−0.92 *	−1.40 *	−1.20 *	−1.25 *

μ_y coefficient of internal friction derived from the onset of non-linearity in $\Delta\sigma$ vs. ϵ_1 curves.
μ_d coefficient of internal friction derived from the onset of dilatancy.
μ_{max} coefficient of internal friction derived from maximum stress differences.
β_y dilation factor at the onset of non-linearity in $\Delta\sigma$ vs. ϵ_1 curves.
β_d dilation factor at the onset of dilatancy.
β_{max} dilation factor at maximum stress difference.
ν Poisson's ration.
G shear modulus.
β dilatancy factor
$(h/G)_{exp}$ experimentally derived ratio of hardening coefficient h and shear modulus G.
$(h/G)_{RR75}$ theoretically predicted ratio of hardening coefficient h and shear modulus G after Rudnicki and Rice, 1975; subscripts refer to coefficient of internal friction used.

increase with either increasing confining pressure (Table 3a; Bernabe and Brace, 1990; Fredrich et al., 1990; Dresen and Evans, 1993), porosity (Table 3b) or particle size (Table 3c). This correspondance indicates first that at confining pressures higher than applied here true work-hardening (i.e., $h > 0$) may be the necessary condition for non-localized deformation; and second that reaching large strains in the ductile field the critical hardening coefficient increases due to the porosity and grain size reduction leading finally to localization, i.e., cataclastic flow is not expected to be a steady state deformation mechanism. The quantitative predictions are improved for the yield vertex model (Table 2 in Rudnicki and Rice, 1975) which takes into account experimentally observed anisotropy of hardening (Celle and Cheatham, 1976). Recently, Diouta et al. (1994) found good agreement between their experimental results and the prediction of a constitutive equation for non-coaxial flow which is equivalent to a yield vertex model.

5.4. Mechanisms related to the transition from brittle failure to cataclastic flow

Dilation during work-hardening and the strong pressure sensitivity of the deformation result from a predominance of cataclastic processes such as microfracturing and relative particle motion. The formation of fracture planes during brittle and transitional deformation may be the result of the coalescence of microfractures (Scholz, 1968; Olsson, 1974b) or the propagation of singular fractures (Lockner et al., 1992) controlled by confining pressure (Schmidt and Huddle, 1976) and microstructural parameters such as grain size and porosity (Hoagland et al., 1973; Rice, 1977, 1981; Wu et al., 1981). The observed dependence of dilatancy coefficients at the brittle–ductile transition (Fig. 8) and the transition pressure (Fig. 10) on initial porosity complement the concept of Edmond and Paterson (1972) for the transition pressure: Continuous inelastic deformation is only possible if sufficient natural porosity is present and/or if porosity develops during homogeneous microfracturing stabilized by the confining pressure.

The particular microfracture mechanisms responsible for the observed deformational behaviour have been addressed in various approaches (discussed by Evans et al., 1990). Rocks can be either described as (a) continua with pores or as (b) granular aggregates: (a) For a continuum with cylindrical pores under triaxial compression Sammis and Ashby (1986) analyze the development and interaction of tensile cracks emanating from the pores due to stress concentrations. Their calculation based on fracture mechanics indicate inhibited crack growth for stress ratios $\lambda < 0.1$. However, brittle behaviour is experimentally observed up to $\lambda \approx 0.2$ (Fig. 11). This overemphasis of the stabilizing role of confining pressure (Wong, 1990; Dresen and Evans, 1993) may be related to the restriction of Sammis and Ashby's model to tensile cracks. Experimental observations demonstrate that first tensile microfractures occurring at tops and bottoms of cylindrical pores cause yielding and then shear fractures initially at pore side walls cause macroscopic failure (Sobolev and Rummel, 1982). From postdeformational microscopic observations Hirth and Tullis (1989) deduce a change in dominance of these two fracture types, tensile at tops and bottoms of pores and shear at pore side walls, at the pressure-induced transition from brittle to ductile behaviour providing a qualitative explanation for the observed decrease in yield strength with increasing confining pressure in the ductile field (Fig. 6; Byerlee, 1968; Miller and Cheatham, 1972).

(b) In models which describe a porous rock as a granular material, the strengthening effect of decreasing porosity is related to the increase of contact area. In rocks of low porosity, failure of individual grains occurs at higher external loads than in rocks of higher porosity (Knudsen, 1959; Friedman, 1976; Gangi, 1976). Failure mechanisms on the grain scale are either tensile cracking at grain surfaces (Hertzian fracture model, e.g. Zhang et al., 1990) or tensile or shear cracking across grains (Brazilian fracture model, e.g. Fairhurst, 1964; Gallagher et al., 1974). The distribution of the load seems to determine the failure mechanism with surfacial crushing near point contacts and bisecting tensile failure for distributed load (Hudson et al., 1972).

Both the Hertzian and Brazilian fracture models yield relations between failure loads of individual grains and their radii; however, the effect of grain size on the failure strength of an aggregate is critically dependent on the relation between externally

applied stresses and resulting loads on grain scale. Using fracture mechanics, Zhang et al. (1990) explicitly derive the pressure at the brittle–ductile transition, σ_{trans}, from hydrostatic compression tests as a function of porosity, grain size, elastic constants and fracture toughness. Their analysis is in qualitative agreement with our observation of decreasing effects of increasing porosity and grain size on transition pressure, but their deduced functional dependence $\sigma_{trans} \propto (\phi \cdot \bar{d})^{-3/2}$ is questionable (Fig. 10; Rutter and Hadizadeh, 1991). Regarding the yield surfaces based on the onset of non-linearity in $\Delta\sigma$ vs. ϵ_1 curves in Fig. 6, it is obvious that the critical pressures, P_{cr}, of hydrostatic irreversible compaction and the mean stress of a triaxial compression test at the brittle–ductile transition, $\bar{\sigma}_{trans}$, are distinguishable points in a $\tau - \bar{\sigma}$ plot. Therefore, P_{cr} and $\bar{\sigma}_{trans}$ cannot be substituted for one another as assumed in the calculations of Zhang et al. (1990). Physically, the difference probably is caused by enhanced compaction due to shear during triaxial loading (Hadizadeh and Rutter, 1983).

Whereas some aspects of the deformational behaviour of porous solids are adequately explained by the micromechanical models discussed above, two major observations are not. First, differences in the post-yield stress difference and hardening coefficients for intact rocks and cold-pressed rocks vanish with increasing confining pressure despite significant differences in initial crack densities (Figs. 3, 5 and 11). Second, stress ratios at the brittle–ductile transition are almost material-independent constants (Fig. 11), although all models use elastic and fracture mechanical properties that vary strongly with mineralogy (Atkinson and Meredith, 1987; Gebrande, 1982; Rummel, 1982). The strengths of intact and thermally granulated marbles also assimilate with increasing confining pressure (Rosengren and Jaeger, 1968; Gerogiannopoulos and Brown, 1978). It follows that neither intragranular fractures nor grain boundary fractures consume much of the deformation energy at moderate to high confining pressures. Therefore, friction probably provides the major energy sink (Bernabe and Brace, 1990) as implied by Byerlee (1968) in his definition for the brittle–ductile transition pressure as the confining pressure for which generation of a fracture plane and frictional sliding on it require identical shear stress. This relation has often been confirmed by experiments (e.g., Gowd and Rummel, 1980; Zhang and Rummel, 1989; Murrell, 1990; Scott and Nielsen, 1991). Friction is the major stress-controlling parameter, the stress ratios at the brittle–ductile transition should be independent of material, because friction coefficients deduced from compression tests are virtually independent of material (e.g. Byerlee, 1968; Rummel, 1982). In addition, when the number of microcracks increases, the degree of work-hardening is related not only to the increased interaction between the cracks but also to the increase in area on which frictional sliding occurs. The non-linear dependence of differential stress, work of deformation, and volumetric strain on inelastic axial strain (e.g. Fig. 2) demonstrates that cataclastic flow is a transient process and necessarily followed by secondary localization (Hirth and Tullis, 1989) when crack density becomes too high.

5.5. Geological implications

Cataclastic flow can be expected to occur in two general geologic situations: first, in places where sediments of high porosities are accumulated under non-hydrostatic conditions like in accretionary wedges; second, in major fault regimes with considerable amount of gouge. Whereas observed transformation pressures of less than 100 MPa for carbonates with porosities as low as 5% indicate that the brittle–ductile transition induced by pressure could, in principle, occur in the Earth's upper crust, the necessary stress ratios deduced from laboratory measurements of about 0.2 to 0.3 seem to be very low. Stress ratios are not porosity dependent for porosities smaller than 25% and only slightly are affected by increasing temperature and decreasing strain rate (e.g. Rutter, 1972). As long as stress depth profiles of active accretionary wedges are not known it can not be judged whether cataclastic flow is pervasive, but from the present experiments it can be concluded that the use of critical state mechanics in interpretations of the mechanical behaviour of accretionary wedges (e.g. Karig, 1990) is an oversimplification for sediments with porosities below about 25%.

Along major faults stress concentrations with stress ratios of about 0.2 to 0.3 are likely to occur locally. Due to the decrease in grain size with increasing strain, gouge work-hardens when deformed

by non-localized cataclastic flow. However, this deformation state is presumably transient and the periodic occurrence of seismic activity may be related to cyclic changes between non-localized flow during stress increase and localized failure with stress drop. Because non-localized cataclastic flow can be accompanied by either volume de- or increase, the conditions for fluid flow in fault gouge and therefore effective stresses may change significantly even during aseismic periods. Such a change in boundary conditions for continuing deformation will complicate the prediction of the mechanical response and requires further exploration.

6. Conclusions

In compression tests at room temperature we observed similar deformational behaviour for cold-pressed and natural porous carbonate rocks. The inelastic response is strongly affected by confining pressure and porosity and to a lesser extent by particle size. Strain rate had no influence. The maximum stress differences increase with increasing confining pressure, decreasing porosity and decreasing particle size. A transition from localized brittle failure to non-localized cataclastic flow occurs with increasing confining pressure, porosity and particle size. Fracture always is associated with dilation, whereas flow can be accompanied by compaction. The transition from brittle failure to cataclastic flow is characterized by:

- Vanishing work hardening, i.e. $h'_{\text{trans}} = 0$, indicating the equivalence of energetic and macroscopic stability.
- Dilatancy coefficients being an increasing function of porosity, $m_{\text{trans}} = f_{(\phi)}$. Dilation for low porosity rocks changes to compaction at higher porosities indicating that a certain amount of free volume — either produced by microfracturing or present as initial porosity — is necessary for the accommodation of the relative movement of grains during cataclastic flow.
- A transition pressure decreasing with porosity and particle size, $\sigma_{\text{trans}} = g_{(\phi,\bar{d})}$.
- Constant stress ratios, $\lambda_{\text{trans}} \approx 0.2$ to 0.3, almost independent of composition and microstructural parameters.
- Decreasing yield strength with increasing confining pressure, i.e. $\mu_\gamma \leq 0$.

The deformation behaviour of the porous carbonates investigated is non-associated and generally not consistent with a critical state concept. Micromechanical approaches show that fracturing on the grain scale is related to the dependences of strength on experimental and microstructural parameters. However, the similarity of strength of natural, intact and cold-pressed rocks at high confining pressures indicates that friction is the dominant sink of deformation energy during cataclastic flow. It is not sufficient to consider a single micromechanism to explain either the onset, continuation and termination of inelastic deformation in a single test or the observation of the deformation fields of fracture and flow.

Acknowledgements

The work was funded by the German Science Foundation (DFG) under contract no. Schr 64/59-1-D2. We are grateful for help and discussions to E. Rybacki, B. Stöckhert, T. Theye and M. Wachmann (RU Bochum), to G. Dresen (GFZ Potsdam) as well as to B. Evans and G. Siddiqi at MIT Cambridge where J. Renner spent a 3-month research period. We gratefully acknowledge the critical comments of T. Engelder, B. Evans, D. Olgaard, E. Rutter and J. Tullis on earlier versions of this paper.

References

Atkinson, B.K. and Meredith, P.G., 1987. Experimental fracture mechanics data for rocks and minerals. In: B.K. Atkinson (Editor). Fracture Mechanics of Rocks. Academic Press, London, pp. 477–525.

Bernabe, Y. and Brace, W.F., 1990. Deformation and fracture of Berea sandstone. Geophys. Monogr., 56. The Heard Volume. Am. Geophys. Union, pp. 91–101.

Brace, W.F., 1961. Dependence of fracture strength of rocks on grain size. Bull. Penn. State Univ. Mineral Industries Experiment Station, 176: 99–103.

Brace, W.F., 1965. Some new measurements of linear compressibility of rocks. J. Geophys. Res., 70: 391–398.

Brace, W.F., Paulding, B.W. Jr. and Scholz, C., 1966. Dilatancy in the fracture of crystalline rocks. J. Geophys. Res., 71(16): 3939–3953.

Budiansky, B. and O'Connell, R.J., 1976. Elastic moduli of a cracked solid. Int. J. Solids Struct., 12: 81–97.

Byerlee, J.D., 1968. Brittle–ductile transition in rocks. J. Geophys. Res., 73(14): 4741–4750.

Celle, C.C. and Cheatham Jr., J.B., 1976. Anisotropic hardening of an initially Isotropic porous Limestone. In: Proc. 17th Symp. Rock Mech., Snowbird, Utah, Aug. 1976, 1A5-1-7.

Chakrabarty, J., 1987. Theory of Plasticity. McGraw-Hill, New York, NY, 791 pp.

Digby, P.J., 1981. The effective elastic moduli of porous granular rocks. J. Appl. Mech., 48: 803–808.

Diouta, N.G., Haied, A., Kondo, D. and Shao, F.J., 1994. Experimental and numerical analysis of strain localization in two rock materials. In: Eurock '94. Balkema, Rotterdam, pp. 93–98.

Dower, R.J., 1967. On the brittle–ductile transition pressure. Acta Metall., 15: 497–500.

Dresen, G. and Evans, B., 1993. Brittle and semibrittle deformation of synthetic marbles composed of two phases. J. Geophys. Res., 98(B7): 10,921–10,933.

Dunn, D.E., LaFountain, L. and Jackson, R.E., 1973. Porosity dependence and mechanism of brittle fracture in sandstones. J. Geophys. Res., 78(14): 2403–2417.

Edmond, J.M. and Paterson, M.S., 1972. Volume changes during the deformation of rocks at high pressures. Int. J. Rock Mech. Min. Sci. Geomech. Abstr., 9: 161–182.

Evans, B., Fredrich, J.T. and Wong, T.-F., 1990. The brittle–ductile transition in rocks: Recent experimental and theoretical progress. In: A.G. Duba, W.B. Durham, J.W. Handin and H.F. Wang (Editors), Geophys. Monogr., 56. The Heard Volume. Am. Geophys. Union, pp. 1–20.

Fairhurst, C., 1964. On the validity of the 'Brazilian' test for brittle materials. Int. J. Mech. Min. Sci. Geomech. Abstr., 1: 535–546.

Fischer, G.J. and Paterson, M.S., 1989. Dilatancy during rock deformation at high temperatures and pressures. J. Geophys. Res., 78(B12): 17,607–17,617.

Fredrich, J.T., Evans, B. and Wong, T.F., 1989. Micromechanics of the brittle to plastic transition in Carrara marble. J. Geophys. Res., 94(B4): 4129–4145.

Fredrich, J.T., Evans, B. and Wong, T.F., 1990. Effect of grain size on brittle and semibrittle strength: Implications for micromechanical modelling of failure in compression. J. Geophys. Res., 95(B7): 10,907–10,920.

Friedman, M., 1976. Porosity, permeability and rock mechanics — A review. In: Proc. 17th Symp. Rock Mech., Snowbird, Utah, Aug. 1976, pp. 2A1-17.

Gallagher, J.J. Jr., Friedman, M., Handin, J. and Sowers, G.M., 1974. Experimental studies relating to microfracture in sandstone. Tectonophysics, 21: 203–247.

Gangi, A.F., 1976. Hertz theory applied to the porosity–pressure, permeability–pressure and failure strength–porosity variations of porous rocks. In: Proc. 17th Symp. Rock Mech., Snowbird, Utah, Aug. 1976, pp. 2A5-1-8.

Gebrande, H., 1982. Elastic wave velocities and constants of elasticity of rocks and rock forming minerals. In: G. Angenheister (Editor), Landolt-Börnstein: Zahlenwerte und Funktionen aus Naturwissenschaften und Technik, Neue Serie, Gruppe 5, Bd. 1b. Springer, Berlin, pp. 1–140.

Gerogiannopoulos, N.G. and Brown, E.T., 1978. The critical state concept applied to rock. Int. J. Mech. Min. Sci. Geomech. Abstr., 15: 1–10.

Gowd, T.N. and Rummel, F., 1980. Effect of confining pressure on the fracture behaviour of a porous rock. Int. J. Mech. Min. Sci. Geomech. Abstr., 17: 225–229.

Hadizadeh, J. and Rutter, E.H., 1983. The low temperature brittle–ductile transition in a quartzite and the occurence of cataclastic flow in nature. Geol. Rundsch., 72: 493–509.

Handin, J. and Hager, R.V. jr, 1957. Experimental deformation of sedimentary rocks under confining pressure: Tests at room temperature on dry samples. Bull. Am. Assoc. Petrol. Geol., 41: 1–50.

Heard, H.C., 1960. Transition from brittle to ductile flow in Solenhofen limestone as a function of temperature, confining pressure and interstitial fluid pressure. In: D. Griggs and J. Handin (Editors), Rock Deformation (A Symposium). Geol. Soc. Am. Mem., 79: 193–226.

Hirth, G. and Tullis, J., 1989. The effects of pressure and porosity on the micromechanics of the brittle–ductile transition in quartzite. J. Geophys. Res., 94(B12): 17,825–17,838.

Hoagland, R.G., Hahn, G.T. and Rosenfield, A.R., 1973. Influence of microstructure on fracture propagation in rock. Rock Mech., 5: 77–106.

Hobbs, B.E., Mühlhaus, H.-B. and Ord, A., 1990. Instability, softening and localization of deformation. In.: R.J. Knipe and E.H. Rutter (Editors), Deformation Mechanisms, Rheology and Tectonics. Geol. Soc. Spec. Publ., 54: 143–165.

Hoshino, K., 1974. Effect of porosity on the strength of the clastic sedimentary rocks. In: Advances in Rock Mechanics, Proc. Third Int. Congr. Rock Mech., IIA: 511–516.

Hudson, J.A., Brown, E.T. and Rummel, F., 1972. The controlled failure of rock discs and rings loaded in diametral compression. Int. J. Rock Mech. Min. Sci. Geomech. Abstr., 9: 241–248.

Hugman, R.H.H. and Friedman, M., 1979. Effects of texture and composition on mechanical behaviour of experimentally deformed carbonate rocks. Am. Assoc. Petrol. Geol. Bull., 63(9): 1478–1489.

Karig, D.E., 1990. Experimental and observational constraints on the mechanical behaviour in the toes of accretionary prisms. In: R.J. Knipe and E.H. Rutter (Editors), Deformation Mechanisms, Rheology and Tectonics. Geol. Soc. Spec. Publ., 54: 383–398.

Khan, A.S., Xiang, Y. and Huang, S., 1991. Behaviour of Berea sandstone under Confining pressure, Part I: Yield and failure surfaces and nonlinear elastic response. Int. J. Plast., 7: 607–624.

Knudsen, F.P., 1959. Dependence of mechanical strength of brittle polycrytalline specimens on porosity and grain Size. J. Am. Ceram. Soc., 42: 376–387.

Kwasniewski, M., 1989. Laws of britle failure and b–d transition in sandstones. In: V. Maury and D. Fourmaintraux (Editors), Rock at Great Depth. Balkema, Rotterdam, pp. 45–58.

Lockner, D.A., Byerlee, J.D., Kuksenko, V., Ponomarev, A. and Sidorin, A., 1992. Observations of quasi-static fault growth from acoustic emissions. In: B. Evans and T.-F. Wong (Edi-

tors), Fault Mechanics and Transport Properties of Rocks. Academic Press, San Diego, CA, pp. 3–31.

Miller, T.W. and Cheatham, J.B. jr., 1972. A new yield condition and hardening rule for rocks. Int. J. Rock Mech. Min. Sci. Geomech. Abstr., 9: 453–471.

Murrell, S.A.F., 1990. Brittle-to-ductile transitions in polycrystalline non-metallic materials. In: D.J. Barber and P. Meredith (Editors), Deformation Process in Minerals, Ceramics and Rocks. Unwin Hyman, Boston, MA, pp. 109–137.

Olsson, W.A., 1974a. Grain size dependence of yield stress in marble. J. Geophys. Res., 79: 4859–4862.

Olsson, W.A., 1974b. Microfracturing and faulting in a limestone. Tectonophysics, 24: 277–285.

Paterson, M.S., 1978. Experimental Rock Deformation—The Brittle Field. Springer, Heidelberg, 294 pp.

Plumb, R.A., 1994. Influence of composition and texture on the failure properties of clastic rocks. In: Eurock '94. Balkema, Rotterdam, pp. 13–20.

Rice, R.W., 1977. Microstructure dependence of mechanical behaviour of ceramics. In: R.K. MacCrone (Editor), Treatise on Materials Science and Technology, Vol. 11. Properties and Microstructure. Academic Press, London, pp. 199–381.

Rice, R.W., 1981. Test-microstructural dependence of fracture energy measurements in ceramics. In: S.W. Freiman and E.R. Fuller jr. (Editors), Fracture Mechanics Methods for Ceramics, Rocks and Concrete, ASTM STP 745. Am. Soc. Test. Mater., pp. 96–117.

Rosengren, K.J. and Jaeger, J.C., 1968. The mechanical properties of an interlocked low-porosity aggregate. Geotechnique, 18: 317–326.

Rudnicki, J.W. and Rice, J.R., 1975. Conditions for the localization of deformation in pressure-sensitive dilatant materials. J. Mech. Phys. Solids, 23: 371–394.

Rummel, F., 1982. Fracture and flow of rocks and minerals. In: G. Angenheister (Editor), Landolt-Börnsteins Zahlenwerte und Funktionen aus Naturwissenschaften und Technik, Neue Serie, Gruppe 5, Bd. 1b. Springer, Berlin, pp. 141–238.

Rutter, E.H., 1972. The influence of interstitial water on the rheological behaviour of calcite rocks. Tectonophysics, 14: 13–33.

Rutter, E.H. and Hadizadeh, J., 1991. On the influence of porosity on the low-temperature brittle–ductile transition in siliciclastic rocks. J. Struct. Geol., 13(5): 609–614.

Sammis, C.G. and Ashby, M.F., 1986. The failure of brittle porous solids under compressive stress states. Acta Metall., 34: 511–526.

Schmidt, R.A. and Huddle, C.W., 1976. Effect of confining pressure on fracture toughness of Indiana limestone. In: Proc. 17th Symp. Rock Mech., Snowbird, Utah, Aug. 1976, pp. 5C3-1-6.

Schock, R.N., Heard, H.C. and Stephens, D.R., 1973. Stress–strain behaviour of a granodiorite and two graywackes on compression to 20 kilobars. J. Geophys. Res., 78(26): 5922–5941.

Schofield, A.N. and Wroth, C.P., 1968. Critical State Soil Mechanics. McGraw-Hill, London.

Scholz, C.H., 1968. Microfracturing and the inelastic deformation of rock in compression. J. Geophys. Res., 73(4): 1417–1432.

Scott, T.E. and Nielsen, K.C., 1991. The effects of porosity on the brittle–ductile transition in sandstones. J. Geophys. Res., 96(B1): 405–414.

Sobolev, G. and Rummel, F., 1982. Shear fracture development and seismic regime in pyrophyllite specimens with soft inclusions. J. Geophys., 51: 180–187.

Veit, K., 1922. Künstliche Schiebungen und Translationen in Mineralien. Neues Jahrb. Mineral., 45: 121–148.

Walsh, J.B., 1965. The effect of cracks on the compressibility of rock. J. Geophys. Res., 70: 381–389.

Walton, K., 1987. The effective elastic moduli of a random packing of spheres. J. Mech. Phys. Solids, 35(2): 213–226.

Wong, T.F., 1990. Mechanical compaction and the brittle–ductile transition in porous sandstones. In: R.J. Knipe and E.H. Rutter (Editors), Deformation Mechanisms, Rheology and Tectonics. Geol. Soc. Spec. Publ., 54: 111–122.

Wu, C.C., Rice, R.W. and Becher, P.F., 1981. The character of cracks in fracture toughness measurements of ceramics. In: S.W. Freiman and E.R. Fuller jr. (Editors), Fracture Mechanics Methods for Ceramics, Rocks and Concrete. ASTM STP 745. Am. Soc. Test. Mater., pp. 127–140.

Zhang, J., Wong, T.F. and Davis, D.M., 1990. Micromechanics of pressure-induced grain crushing in porous rocks. J. Geophys. Res., 95(B1): 341–352.

Zhang, L. and Rummel, F., 1989. Shear fracture energy of rock at high pressure and high temperature. Phys. Chem. Earth, 17: 99–109.